Journal of Catalysis 266 (2009) 15–25

Contents lists available at ScienceDirect

Journal of Catalysis

journal homepage: www.elsevier.com/locate/jcat

Sulfur resistance enhancement by grafted TiO_2 in SiO_2-supported Pd catalysts: Role of grafted TiO_2 and genesis of Pd clusters

Hwo-Shuenn Sheu [a], Jyh-Fu Lee [a], Shin-Guang Shyu [b], Wha-Wen Chou [c], Jen-Ray Chang [c,*]

[a] National Synchrotron Radiation Research Center, Hsinchu, Taiwan
[b] Institute of Chemistry, Academia Sinica, Nankang, Taipei, Taiwan
[c] Department of Chemical Engineering, National Chung Cheng University, Chia-Yi, Taiwan

ARTICLE INFO

Article history:
Received 23 January 2009
Revised 27 April 2009
Accepted 10 May 2009
Available online 9 June 2009

Keywords:
Pd catalysts
Sulfur poisoning
Deactivation
X-ray absorption spectroscopy
IR
Grafted TiO_2

ABSTRACT

Pd clusters on TiO_2-grafted SiO_2 (TiO_2–SiO_2), SiO_2, and TiO_2 particles were prepared via impregnation with palladium (II) acetate followed by air calcination and hydrogen reduction. The prepared catalysts were tested by tetralin hydrogenation with sulfur-poisoning reaction. The results show that Pd/TiO_2–SiO_2 presents the highest activity maintenance. To investigate the role of the grafted TiO_2 in improving the activity maintenance, the catalyst samples were characterized by FT-IR, EXAFS, and XRD. The results indicated that layer-like TiO_2 clusters formed on SiO_2 help anchoring palladium oxides during air calcination. This anchoring leads to the formation of relatively small Pd clusters having less electronic density as opposed to the other two catalysts. Combining structural characterization with kinetic study results, we concluded that the superior catalytic performance for Pd/TiO_2–SiO_2 could arise from the decrease of the affinity of Pd for H_2S and the increase of hydrogen reducibility for PdS_2.

1. Introduction

The interactions between noble-metal clusters and non-reducible metal–oxide carriers are highly important for supported metal catalysts [1–3]. The interactions and the catalytic properties of these materials could be modified by the addition of TiO_2 [4,5]. However, little is known about the role of TiO_2 in changing the catalytic properties because of the difficulty in characterizing metal–support interface. In this research, the genesis of the Pd clusters on TiO_2-grafted SiO_2 was explored by the unique use of X-ray absorption spectroscopy [3,6,7]. The results indicated that TiO_2 helps anchoring PdO_x during air calcination and maintaining it in small ensembles during H_2 reduction. This observation is expected to illuminate how TiO_2 on the catalyst support influences the structure and catalytic properties, specifically sulfur resistance of the catalysts.

To facilitate this study, a material system was carefully designed. In the system, Pd was the metal of choice because it is used widely as the active site for catalytic reactions [1,8–11]. Palladium (II) acetate was chosen because the Pd precursors readily undergo cleavage on metal–oxide carriers offering opportunities to prepare highly dispersed Pd catalysts [9,12]. TiO_2-grafted silica was chosen as the support (or carrier) because it presents a high surface area and a higher thermal stability than pure TiO_2 toward sintering at a high temperature. Higher dose of Pd precursor and, in turn, Pd clusters can be expected to bond to TiO_2 on this composite support. Hence, the EXAF (Extended X-ray absorption fine structure) measurement can be performed in the transmission mode, which presents a much higher signal-to-noise ratio than the fluorescence mode; thus the contribution of TiO_2–PdO_x interaction in EXAFS spectrum would not be affected significantly by noise. Moreover, since the catalyst samples are air and moisture sensitive, EXAFS measurements were carried out in an in-situ EXAFS cell, which is free of air and moisture.

In order to illustrate the merit of the grafted TiO_2 in catalysis, sensitivity to sulfur poisoning was tested because (1) supported Pd catalysts are very sensitive to sulfur compound [13], (2) maintaining the required level of sulfur to avoid deactivation in commercial operation is very expensive and millions of dollars are lost every year in chemical and oil industries as a consequence of sulfur poisoning [14], and (3) several methods including the use of acidic supports [15–17], the addition of a second metal [17–20], and the exchange of NaY support with polyvalent cations [21,22] have been used to enhance the sulfur resistance of supported metal catalysts, whereas no information regarding the use of TiO_2–SiO_2 supports has been reported.

2. Experimental

2.1. Preparation of TiO_2–SiO_2

The samples were prepared by incipient-wetness impregnation technique. Silica (MN Kieselgel 60, surface area of 400 m^2/g, particle

* Corresponding author. Fax: +886 5 2721206.
E-mail addresses: chmjrc@ccu.edu.tw, chmjrc@ccunix.ccu.edu.tw (J.-R. Chang).

0021-9517/$ - see front matter © 2009 Elsevier Inc. All rights reserved.
doi:10.1016/j.jcat.2009.05.008

size of 0.2–0.5 mm, MACHEREY-NAGEL) was pre-dried in an oven at 120 °C for 24 h in order to remove the water. The silica was brought in contact with a toluene solution of titanium isopropylate $Ti(OCH(CH_3)_2)_4$ (Acros) in a glove box. The amount of titanium isopropylate added to silica was such that the resulting solid contained 7 wt% TiO_2. The toluene solvent was removed by evacuation for 4 h at room temperature, and the resulting solid was calcined under air at 450 °C for 4 h. The sample after the calcination was denoted as TiO_2–SiO_2.

2.2. Preparation of Pd/TiO_2, Pd/TiO_2–SiO_2, and Pd/SiO_2

Pd/TiO_2–SiO_2 and Pd/SiO_2 were prepared according to the method reported by Lin and Chou and our previous paper [9,23]. Palladium acetate, $Pd(Ac)_2$, of 0.64 g was dissolved in 200 mL of toluene with stirring for 3 h, and 15 g of TiO_2–SiO_2, SiO_2, or TiO_2 (Merck, surface area of 40 m^2/g, average crystal grain size <100 nm) support was then added. The toluene was removed by filtration followed by evacuation. The resulting samples were denoted as $Pd(Ac)_2/TiO_2$–SiO_2, $Pd(Ac)_2/SiO_2$, and $Pd(Ac)_2/TiO_2$ for TiO_2–SiO_2, SiO_2, and TiO_2 supports, respectively. After calcinations at 450 °C in flowing air for 3 h, the samples were denoted as PdO_x/TiO_2–SiO_2, PdO_x/SiO_2, and PdO_x/TiO_2. All samples were stored in a nitrogen-filled glove box before FT-IR and X-ray absorption characterization.

For measuring Pd content, 0.2 g ground catalyst sample was transferred to a crucible, wetted with 1 mL water, and mixed with 10 mL UA-1 (HCl- and HF-containing acid-dissolution reagent, Inorganic Ventures Inc.) and 1 mL 12 N HNO_3. The slurry was stirred and heated to just below the boiling point until the catalyst had completely dissolved. After the solution was cooled to room temperature, 50 mL UNS-1 (Inorganic Ventures Inc.) was added, and the solution was transferred to a 100-mL flask. After allowing the solution to stand for 5 min, the solution was further diluted with water to 100 mL. Pd loading was then measured by inductively plasma optical emission measurement (Perkin Elmer PE Optima 4300), and the results are summarized in Table 2.

2.3. Characterization of catalyst samples by infrared spectroscopy

FT-IR (Fourier-transform infrared) spectroscopy characterizing CO adsorbed on the Pd catalysts was performed with a Shimadzu IR Prestige-21 equipped with a MCT detector. The wafer samples were prepared and loaded into an IR cell in a N_2-filled glove box. The cell was connected to a vacuum/gas-handling manifold for in-situ treatment. The reduction of the samples was carried out by flowing H_2 at 200 °C for 1 h. After the reduction, the sample was cooled to room temperature, and CO (flowing at 50 mL/min at 1 atm) was introduced into the cell and was maintained for about 20 min. After the CO treatment, the cell was evacuated to a pressure of approximately 10^{-2} to 10^{-3} Torr, and IR spectra having a 2 cm^{-1} spectral resolution were recorded.

2.4. Transmission electron microscopy

The reduced Pd catalyst samples were carefully pulverized, dispersed in ethanol, fetched on Cu grids, and then dried for later TEM (Transmission electron microscopy) analysis. The TEM (Philips, TECNAI 20) is typically operated at 200 KeV.

2.5. X-ray absorption spectroscopy

The X-ray absorption measurements of Pd *K*-edge (24,350 eV) were performed on the super-conducting wavelength shifter (SWLS) beamline BL01C1 at the National Synchrotron Radiation Research Center (NSRRC) in Hsinchu, Taiwan, with an energy from 5 to 33 KeV. The monochromator employs double Si(1 1 1) crystals for energy selection with a resolution ($\Delta E/E$) better than 2.5×10^{-4}. It was detuned 20% at E_0 + 50 eV to suppress a higher harmonic radiation. The monochromator was scanned at an energy from 200 eV below the palladium *K* absorption edge (24,350 eV) to 1000 eV above the edge. Each sample was pressed into a self-supporting wafer in a N_2-filled glove box and was then placed into an EXAFS cell. The cell was connected to a vacuum/gas-handling manifold for in-situ treatment. All samples were measured in a transmission mode at room temperature. The transmission measurement geometry was arranged using gas-filled ionization chambers to monitor the intensities of the incident and transmitted X-rays. To gain the proper absorption ratio for the incoming X-rays, the gas compositions in the ionization chambers were selected at an argon to nitrogen mole ratio of 1/1 for the first chamber and as pure argon for the second chamber, respectively. After the measurement of the supported PdO_x sample, the temperature was increased from room temperature at about 10 °C/min to 200 °C with the flow of hydrogen. After the temperature reached the setting temperature, it was maintained for 0.5 h. Then the cell was allowed to cool in liquid nitrogen to room temperature, and the EXAFS spectrum was measured again. The samples after the reduction were denoted as Pd/TiO_2–SiO_2, Pd/SiO_2, and Pd/TiO_2. To investigate the effects of Pd morphology on sulfur poisoning and hydrogen reactivation, the hydrogen-reduced Pd/TiO_2–SiO_2 and Pd/SiO_2 samples were first treated by flowing 10,000 ppm H_2S containing N_2 for 30 min. After data collection, the sulfur-poisoned samples were reactivated by flowing hydrogen at 200 °C for 30 min. After the cell was cooled to room temperature, the EXAFS spectrum was measured again.

X-ray absorption spectra of Ti *K*-edge (4966 eV) were recorded on the wiggler beamline BL17C at NSRRC. Two Rh-coated mirrors (mainly for the purpose of collimating and focusing the synchrotron beam) were used to eliminate the high energy components. However, the cut-off energy was set to 15 keV for both mirrors so that the third harmonics from Si(1 1 1)-crystal monochromator may not be *completely* rejected by the mirrors when the fundamental photon energy was scanned around Ti *K*-edge (~5 keV). Accordingly, the higher X-ray harmonics were minimized by detuning at E_0 + 50 eV. The ion chambers used for measuring the incident (I_0) and transmitted (I) synchrotron beam intensities were filled with a mixture of N_2 and He gases and a pure N_2 gas, respectively.

$Ti(OCH(CH_3)_2)_4$, $Ti(OCH(CH_3)_2)_4$ adsorbed on SiO_2, and TiO_2–SiO_2 samples were mixed with some powders of boron nitride (which is almost transparent to X-ray) before being pressed into wafers with a uniform thickness. The TiO_2 content in our Pd/TiO_2–SiO_2 sample was about 7 wt%, which was just high enough for the transmission measurements to be possible.

2.6. Synchrotron XRD

Powder X-ray diffraction (PXRD) was performed at the BL01C2 beamline of the NSRRC with the wavelength of 0.9537 Å (13 keV). Two-dimensional diffraction patterns were recorded by a Mar345 imaging plate system with a sample-to-detector distance of 300 mm. Diffraction angle was calibrated with Si powders (NBS640b) and silver behenate. One-dimensional XRD profiles were integrated from selected fan-like areas of the symmetrical 2-D powder rings using the Fit2D program [24]. The crystalline grain sizes were obtained from the commonly used Scherrer's equation: $t = k\lambda/(B\cos\theta)$, with the crystal grain size t, shape correction constant $k = 0.9$ for spherical particle, and FWHM of the related Bragg peaks B [25].

2.7. Data analysis

Data reduction and data analysis were performed with the XDAP code developed by Vaarkamp et al. [26]. Standard procedures were

followed to extract the EXAFS data from the measured absorption spectra. The pre-edge was approximated by a modified Victoreen curve [7], and the post-edge background was subtracted using cubic spline routines [7]. Normalization was performed by dividing the data by the height of the absorption edge at 50 eV above the edge. For Pd samples, a k^2-weighted Fourier transformation without correction was performed on the EXAFS function over the range $3.5 < k < 14$ Å^{-1}. The major contributions were isolated by inverse Fourier transformation of the data in the range $1.0 < R < 3.8$ Å. The coarse structural parameters characteristic of the Pd–Pd contribution were determined by fitting the k^2-weighted Fourier-isolated EXAFS function in the range $7.0 < k < 13.0$ Å^{-1}; the Pd–O, Pd–Ti, and Pd–S contributions in this region were small. An EXAFS function calculated from these parameters was then subtracted from the raw data (Fourier-isolated EXAFS function). Such a residual spectrum was expected to represent the contributions of metal–support interactions, palladium oxides, and palladium sulfides. The main peaks of the residual spectrum were isolated by Fourier filtering, and the backscatter atoms characterizing the isolated EXAFS spectra were identified by comparing the amplitude function of the EXAFS spectra with that of Pd–X calculated from FEFF [27], where X is the possible backscatter atoms. The structural parameters characteristic of the contributions of the metal–support interface (Pd–Ti), Pd–O, and Pd–S were then estimated by fitting the resulting spectrum obtained from the subtraction of the Pd–Pd contributions from the raw data. The structural parameters obtained from the recursive iteration method were then used as the initial guess for the nonlinear least-square multiple-shell fitting routine.

Data analysis procedure for the Ti samples is similar to that for the Pd samples. The structural parameters of Ti–O and Ti–Ti contributions were first estimated by calculating the EXAFS function that agrees as closely as possible with the experimental EXAFS results in r space ranging from 1.0 to 3.5 Å. Contributions of TiO_2–SiO_2 interaction (Ti–Si) were then estimated by fitting the resulting spectrum obtained from the subtraction of the Ti–O and Ti–Ti contributions from the raw data. The obtained parameters were then used as the initial guess for the nonlinear least-square multiple-shell fitting routine.

The EXAFS contributions for Pd–Pd were analyzed with phase shifts and backscattering amplitudes obtained from the EXAFS data for Pd foil. The Ti–Ti, Ti–O, Ti–Si, Pd–S, Pd–O, and Pd–Ti were analyzed with phase shifts and backscattering amplitudes calculated from FEFF.

2.8. Tests of sulfur-poisoning catalyst deactivation

Catalyst deactivation tests were carried out in a continuous downflow fixed-bed reactor. The reactor was a stainless-steel tube with an inner diameter of 1.2 cm. It was heated electrically, and the temperature was controlled by a PID temperature controller with a thermocouple at the outer wall of the reactor. The temperature difference between the outer wall of the reactor and the center of the catalyst bed was about 10 °C. The upstream part of the reactor was filled with particles of a catalytically inactive ceramic material for preheating and inhibition of channeling effects. The reaction system was first purged with dry nitrogen gas (Sun-Fu, 99.99%) for 2 h. Catalyst samples (sphere of 200–500 μm diameter) of 1.5 g (about 2 mL) were diluted with inert ceramic (sphere of about 500–1000 μm diameter) in a ratio of 1:5, and were then reduced at 200 °C with the flow of pure hydrogen for 0.5 h. After reduction, the test was carried out under the following conditions: weight hourly space velocity (WHSV), 12.0 g of feed/h * g of catalyst; H_2/tetralin mole ratio, 7.0; and pressure, 3.24 MPa. Tetralin with 200 ppm of sulfur was used as the feed. Tetralin (Merck) was dried with particles of activated 4 A molecular sieve, and was then mixed with a certain amount of benzothiophene to prepare the feed. Liquid products were trapped by a condenser at −5 °C. Samples were collected periodically and were analyzed by GC and GC/mass spectrometry. The product gas stream was analyzed by gas chromatography. The GC/mass spectrometry system used for feed and product analysis was a Shimadzu Model GC-17A-GCMS: QP5050(A) equipped with a BP1 (100% dimethyl polysiloxane) capillary column. The column was operated at 40–200 °C with a ramping rate of 10 °C/min and a flow rate of 50 mL/min of dry He. The GC system used for analysis was Shimadzu Model GC-14B with a FID detector. The column and operating conditions were the same as those for GC/mass spectrometry.

Ninety-eight percent of the feed was recovered as the reaction products, as estimated by the material balance calculations. Carbon balance was performed based on the material balance and GC results, and the results indicated that 98 ± 1% of carbon balance was reached. The 2% loss was attributed to the hydrocarbon deposited on the wall of the reaction system, on the catalyst, and on the surface of the ceramic reactor packing.

In order to remove the sulfur contamination from the reaction apparatus, the reactor was treated by heating at 600 °C for 8 h in flowing air. Since the reactor is made of stainless steel 316, sulfur, or more precisely, hydrogen sulfide formed during the reaction causes the formation of iron sulfide according to the balanced reaction:

$$H_2S + Fe \rightarrow FeS + H_2$$

When the apparatus was treated at 600 °C in flowing air, the ferrous sulfide was oxidized into ferric sulfate and then decomposed into ferric oxide Fe_2O_3 and sulfur oxides (SO_2 and SO_3). The sulfur oxides thus formed were removed by NaOH scrubbing, and the red ferric oxide was removed by brushing.

3. Results and discussion

3.1. Accelerated sulfur-poisoning catalyst deactivation

Total tetralin conversion for the sulfur-containing feed is shown as a function of time on stream in the flow reactor (Fig. 1). The conversion of Pd/TiO_2 dropped rapidly right after the test began, and the catalyst lost all its activity at about the third hour of the run. Different from Pd/TiO_2, two stages of deactivation were observed for Pd/TiO_2–SiO_2 and Pd/SiO_2 catalysts. The first stage started right after the introduction of feed into the reaction system, and extended until the time on stream at which the deactivation rate becomes lower.

The second stage began when the deactivation rate increased again with time on stream, which was about 3 and 5 h on stream for Pd/SiO_2 and Pd/TiO_2–SiO_2, respectively. Compared with Pd/SiO_2, the first-stage deactivation for Pd/TiO_2–SiO_2 extended longer, and in the nearly steady state (about 10 h on stream) the catalyst maintained a higher activity.

In the characterization of the reaction products, cis- and trans-naphthalene were detected by GC/mass spectrometry indicating that tetralin was converted to decahydronaphthalene

$$\text{Tetralin} + H_2 \leftrightarrow \text{trans-decahydronaphthalene} + \text{cis-decahydronaphthalene}$$

Our previous works reported that 90% of benzothiophene is catalytically converted to ethylbenzene, styrene, and H_2S over Pt/Al_2O_3 catalyst at 270 °C and at 32 atm, and that the conversion is insensitive with time on stream after the induction period [28]. In the experiment described here, besides ethylbenzene, ethylcyclohexane was detected in liquid products suggesting that ethylbenzene is further hydrogenated to ethylcyclohexane

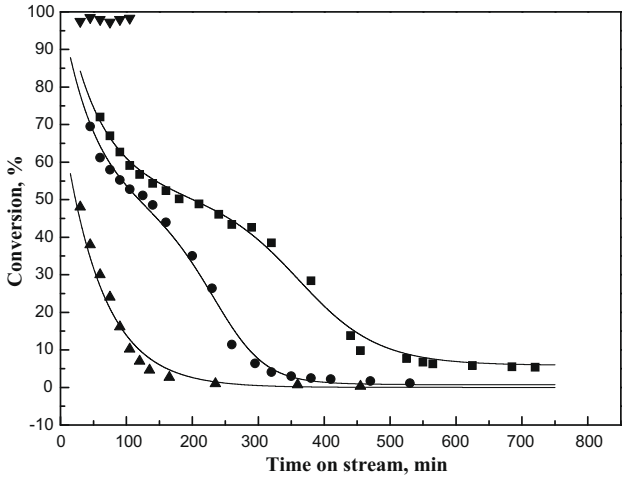

Fig. 1. Aging tests for Pd catalysts run at WHSV of 12.0, 200 °C, and 32 atm with 200 ppm of sulfur-containing tetralin feed: ■, $Pd/TiO_2–SiO_2$; ●, Pd/SiO_2; ▲, Pd/TiO_2; solid line, data calculated from proposed model; ▼, pure tetralin feed catalyzed by $Pd/TiO_2–SiO_2$ for comparison.

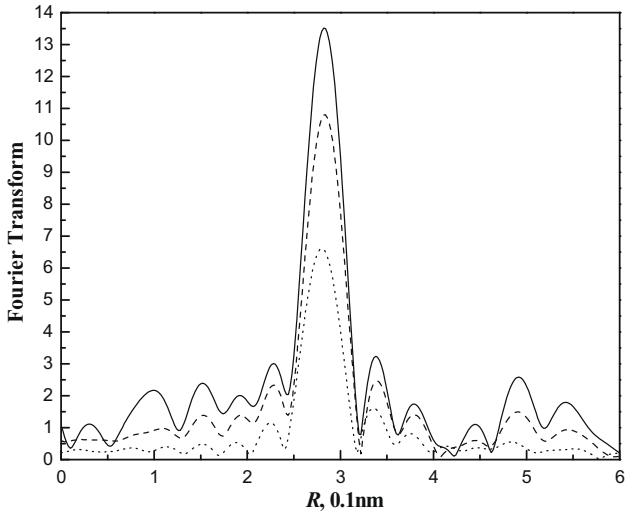

Fig. 2. Magnitude of the EXAFS Fourier transform ($3.5 < k^2 < 12.0$, Pd–Pd phase and amplitude corrected) for Pd/TiO_2 (solid line), Pd/SiO_2 (dashed line), and $Pd/TiO_2–SiO_2$ (dotted line).

$$\text{Benzothiophene} + 5/2H_2 \rightarrow \text{ethylbenzene} + H_2S$$
$$\text{Ethylbenzene} + 5/2H_2 \rightarrow \text{ethylcyclohexane}$$

Since only a trace of styrene was detected and no significant catalyst deactivation was observed for pure tetralin feed (Fig. 1), sulfur poisoning was suggested to be the main factor of the catalyst deactivation.

3.2. Structure of $Pd/TiO_2–SiO_2$, Pd/SiO_2, and Pd/TiO_2

Fourier-transformed EXAFS functions at the Pd *K*-edge provide the qualitative information on the structure of Pd clusters. As shown in Fig. 2, the Pd–Pd phase- and amplitude-corrected Fourier- transformed EXAFS functions in*r* space of the three hydrogen-reduced samples show that the peak corresponding to the first Pd–Pd shell (at about 2.7 Å) for the $Pd/TiO_2–SiO_2$ was much lower than that for Pd/SiO_2 and for Pd/TiO_2. Since the intensity of the Fourier-transformed EXAFS functions is proportional to the coordination number [7], this result indicates that much smaller Pd clusters were formed on $TiO_2–SiO_2$. The detailed analysis of the EXAFS data confirmed this result (Table 1). The coordination numbers of the first Pd–Pd shell were 5.7, 7.8, and 10.2 for $Pd/TiO_2–SiO_2$, Pd/SiO_2, and Pd/TiO_2, respectively.

The higher-shell data provide a basis for the determination of Pd morphology. The Fourier transforms indicated the presence of a peak at approximately 3.8 Å. The distance is consistent with the second shell of bulk fcc Pd, as reflected by the crystallographic data, and is an indication of the Pd clusters of three-dimensional character [29]. The results suggest that Pd clusters with structures resembling spheres (sphere-like clusters) formed on the support, and that the morphology of Pd clusters on the support $TiO_2–SiO_2$ can thus be determined by the first shell Pd–Pd coordination number. For $Pd/TiO_2–SiO_2$ catalyst, the Pd–Pd coordination number of 5.7 suggests that the average diameter of the Pd clusters is about 11 Å, and that the fraction of atoms on the surface is about 85%. If Pd clusters are bounded by a (1 1 1) face in the metal–support interface, a (1 1 1) interface only allows up to three Pd–O bonds per Pd interface atoms. The $Pd–O_{support}$ coordination of 0.7 suggests that about 20% of Pd atoms existed at the interface between Pd clusters and $TiO_2–SiO_2$; if Pd clusters are bounded by a (100) face, the fraction of Pd atoms at interface is about 17%.

The Pd/SiO_2 and Pd/TiO_2 samples were characterized by a first shell Pd–Pd contribution with coordination numbers of 7.8 and 10.2, respectively. These values with the evidence provided by the presence of the second shell Pd–Pd contribution suggest that the average cluster size and fraction of atoms on surface are about 22 Å and 64%, respectively, for Pd/SiO_2, and are about 100 Å and 24%, respectively, for Pd/TiO_2. Moreover, no significant peak characterizing $Pd–O_{support}$ contributions was observed, suggesting that the metal–support interactions for these two catalysts are rather small.

A meaningful cluster size distribution of the three samples was characterized by TEM, and their micrographs which can represent the cluster size distribution are shown in Fig. 3. The average Pd clusters are about 150, 25, and 15 Å for Pd/TiO_2, Pd/SiO_2, and $Pd/TiO_2–SiO_2$, respectively. The results are qualitatively consistent with EXAFS results, whereas they are higher than those estimated by EXAFS because our TEM facility was unable to characterize Pd clusters with a diameter less than 10 Å.

CO volumetric experiments were performed in micromeritics ASAP 2010, and the results showed that 1.8, 1.4, and 0.7 mL/g of CO adsorbed on the $Pd/TiO_2–SiO_2$, Pd/SiO_2, and Pd/TiO_2, respectively. The values combined with the ratio of the bridged to terminal CO intensity characterized by FT-IR indicate that the fraction of atoms on the surface can roughly be estimated. If we assume that the terminal CO bonded to one Pd atom while the bridged CO bonded to two Pd atoms, the calculated results are slightly higher than those estimated from EXAFS and TEM (Table 2), whereas if we assume that only one CO bonded to one surface atom, the results are much lower than those estimated by EXAFS and TEM.

3.3. Thermal stability of TiO_2 nanoparticles and $TiO_2–SiO_2$: XRD results

PXRD patterns of anatase TiO_2 were measured at various calcination temperatures as shown in Fig. 4a. TiO_2 nanoparticles were prepared by hydrolysis of titanium (IV) butoxides in water at 70 °C [30]. The particles were aggregated during calcination. The crystal grain sizes of TiO_2 calculated according to Scherrer's equation were 16, 19, 24, 36, and 80 nm for the sample calcined at 300, 350, 450, 550, and 650 °C in air for 2 h, respectively. Moreover, PXRD patterns clearly indicate that the material undergoes phase change at about 550 °C.

In contrast to the laboratory-prepared TiO_2, no significant TiO_2 aggregation was observed for the commercial anatase (surface area of 40 m^2/g, average grain size <100 nm) during calcination up to 550 °C (Fig. 4b). Since this temperature (550 °C) is well above the

Table 1
(a) Summary of EXAFS analysis results of Ti edge for $Ti(OCH(CH_3)_2)_4$ adsorbed on SiO_2 and TiO_2–SiO_2. (b) Summary of EXAFS analysis results of Pd edge for Pd and PdO_x samples.

Shell	N[a]	R[b] (Å)	$1000 \times \Delta\sigma^{2}$[c] (Å^2)	ΔE_0[d] (eV)	EXAFS reference
(a)					
$Ti(OCH(CH_3)_2)_4$ adsorbed on SiO_2					
Ti–O	4.4 ± 0.4	1.86 ± 0.05	15 ± 1	14 ± 1	Ti–O
Ti–Ti	0.5 ± 0.3	3.19 ± 0.04	0 ± 5	−2 ± 4	Ti–Ti
Ti–Si	2.4 ± 0.4	2.81 ± 0.02	18 ± 2	6 ± 1	Ti–Si
TiO_2–SiO_2					
Ti–O	3.9 ± 0.1	1.91 ± 0.01	11 ± 1	9.7 ± 0.4	Ti–O
Ti–Ti	3.0 ± 0.8	3.17 ± 0.03	13 ± 4	−9 ± 2	Ti–Ti
Ti–Si	2.4 ± 0.3	2.90 ± 0.01	4 ± 2	−3 ± 1	Ti–Si
(b)					
Pd/TiO_2					
Pd–Pd	10.2 ± 0.3	2.83 ± 0.01	8 ± 1	7.0 ± 0.3	Pd–Pd
Pd/SiO_2					
Pd–Pd	7.8 ± 0.3	2.81 ± 0.01	8 ± 1	5.4 ± 0.4	Pd–Pd
Pd/TiO_2–SiO_2					
Pd–Pd	5.7 ± 0.3	2.78 ± 0.01	9 ± 1	6.6 ± 0.6	Pd–Pd
Pd–$O_{support}$	0.7 ± 0.2	2.25 ± 0.09	13 ± 3	−13 ± 9	Pd–O
PdO_x/TiO_2					
Pd–O	3.4 ± 0.1	2.02 ± 0.01	2.0 ± 0.2	4.9 ± 0.2	Pd–O
Pd–Pd	5.4 ± 0.5	3.11 ± 0.01	5.0 ± 0.3	−1.5 ± 0.3	Pd–Pd
PdO_x/SiO_2					
Pd–O	2.8 ± 0.1	2.00 ± 0.01	2.0 ± 0.2	8 ± 1	Pd–O
Pd–Pd	3.9 ± 0.1	3.01 ± 0.01	4.9 ± 0.3	−1.2 ± 0.2	Pd–Pd
PdO_x/TiO_2–SiO_2					
Pd–O	2.9 ± 0.2	2.00 ± 0.02	3 ± 1	8 ± 1	Pd–O
Pd–Pd	1.8 ± 0.4	3.01 ± 0.02	9 ± 1	13 ± 2	Pd–Pd
Pd–Ti	0.7 ± 0.2	3.43 ± 0.04	2 ± 1	6 ± 3	Pd–Ti
Pd–Si	1.8 ± 0.2	3.31 ± 0.03	5 ± 2	7 ± 1	Pd–Si
Pd/SiO_2 after H_2S treatment					
Pd–S	1.5 ± 0.2	2.32 ± 0.02	5 ± 1	1 ± 1	Pd–S
Pd–Pd	3.2 ± 0.2	2.73 ± 0.01	7 ± 1	7.3 ± 0.8	Pd–Pd
Pd/SiO_2 after H_2S treatment followed by hydrogen reactivation					
Pd–S	1.4 ± 0.2	2.33 ± 0.02	8 ± 1	2 ± 1	Pd–S
Pd–Pd	4.6 ± 0.4	2.77 ± 0.01	9 ± 1	6.0 ± 0.2	Pd–Pd
Pd/TiO_2–SiO_2 after H_2S treatment					
Pd–S	0.7 ± 0.2	2.34 ± 0.02	3 ± 1	−2 ± 1	Pd–S
Pd–Pd	3.2 ± 0.3	2.71 ± 0.02	9 ± 1	5.4 ± 0.3	Pd–Pd
Pd–O	0.6 ± 0.2	2.07 ± 0.02	4 ± 2	−1 ± 1	Pd–O
Pd/TiO_2–SiO_2 after H_2S treatment followed by hydrogen reactivation					
Pd–S	0.2 ± 0.1	2.36 ± 0.02	0 ± 3	0 ± 2	Pd–S
Pd–Pd	5.1 ± 0.2	2.77 ± 0.01	9 ± 3	8.2 ± 0.3	Pd–Pd
Pd–O	0.5 ± 0.2	2.05 ± 0.03	7 ± 3	−2 ± 1	Pd–O

[a] N, the coordination number for the absorber–backscattering pair.
[b] R, the average absorber–backscattering distance.
[c] $\Delta\sigma^2$, the difference in Debye–Waller factors between sample and standard.
[d] ΔE_0, the inner potential correction.

operation temperature for preparing Pd catalyst, the TiO_2 aggregation has no effects on the morphology of Pd clusters. Hence, commercial anatase was used for the preparation of Pd/TiO_2 catalysts.

The SiO_2 support was calcined up to 900 °C. Fig. 5a shows the PXRD characterization patterns. No crystalline signals were found for these samples indicating that SiO_2 maintains its amorphous state even at a high temperature, which would be advantageous for applications as a catalyst support. Similar thermal treatments were performed for TiO_2–SiO_2, and the PXRD patterns of TiO_2–SiO_2 show that the TiO_2 maintains its amorphous states at the temperature up to 600 °C (Fig. 5b). Hence, highly dispersed Pd clusters could be prepared on TiO_2–SiO_2, which has a high surface area and thermal stability.

3.4. Characterization of grafting TiO_2 on SiO_2 by EXAFS

Some important structural information can be obtained from the Fourier transform of the EXAFS functions, even without a detailed quantitative EXAFS analysis. Fig. 6 shows the Ti–O phase-corrected Fourier-transformed EXAFS function at the Ti edge characterizing $Ti(OCH(CH_3)_2)_4$. $Ti(OCH(CH_3)_2)_4$ adsorbed on SiO_2, and TiO_2–SiO_2. For the $Ti(OCH(CH_3)_2)_4$ sample, the peak at a distance of about 1.8 Å is contributed from the Ti–O contribution, and the peaks at the distance between 3.0 and 4.5 Å are contributed from the Ti–C contributions.

During the impregnation, the hydroxyl groups on the SiO_2 surface reacted with isopropoxide ligands, hence, diminishing the amplitude of the peaks at the distance between 3.0 and 4.5 Å, and the shifting of the position peak at a distance of about 1.8–1.9 Å was observed. Detailed EXAFS analysis further showed that the resulting material had average Ti–O and Ti–Si bond distances of 1.86 and 2.81 Å, and coordination numbers of 4.4 and 2.4, respectively. The results suggested that the silanol groups on silica surface react with titanium alkoxyl groups to produce Ti–O–Si linkages.

After the calcination of $Ti(OCH(CH_3)_2)_4$ adsorbed on SiO_2, the amplitude of the peaks at about 3.0 Å increased concomitantly

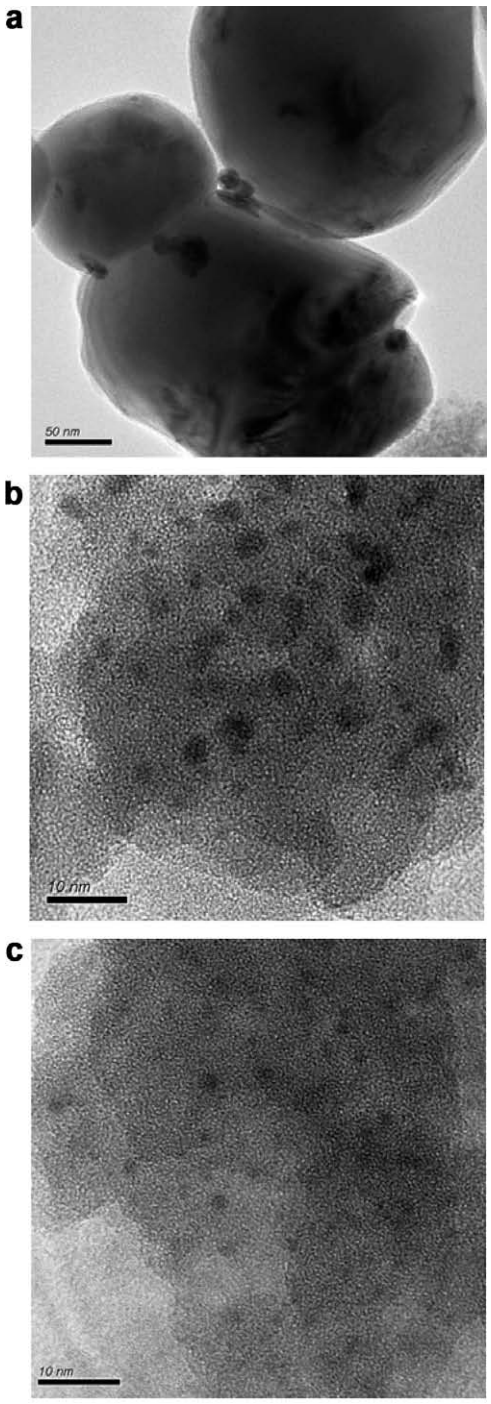

Fig. 3. TEM photographs of (a), Pd/TiO_2; (b), Pd/SiO_2; and (c), Pd/TiO_2–SiO_2.

with the appearance of two more peaks at about 3.6 and 5.4 Å, which are consistent with the second shell of Ti–O and Ti–Ti, respectively.

Comparisons of Fourier transform of EXAFS data between TiO_2–SiO_2 and commercial anatase (Fig. 7b) show that there are no significant higher-shell contributions with a distance higher than 5.5 Å being observed. These results suggest that small TiO_2 clusters were formed on the SiO_2 surface.

As shown in Fig. 7a, the data quality is good. The useful data range was sufficient to allow and estimate the 12 parameters of three principle EXAFS contributions (Table 1); the statistically justified number of parameters is approximately 15, which is esti-

Table 2
Summary of surface characterization results.

Catalyst	Pd/TiO_2–SiO_2	Pd/SiO_2	Pd/TiO_2
Pd (wt%)	1.68	1.62	1.96
Chemisorption[a] (μmol CO/mg Pd)	4.5	3.6	1.4
TEM (nm)	1.0–2.0, d_{mean} = 1.5	1.4–3.3, d_{mean} = 2.5	5–22, d_{mean} = 15
EXAFS (nm)	1.1	2.2	10
D_{TEM} (%)	70	50	–
D_{EXAFS} (%)	77	64	24
$D_{CO_{chemisorption}}$ (%)	85	69	30

d_{mean}: mean diameter of Pd clusters.
D_{EXAFS}: fraction of atoms on the surface of Pd clusters calculated from EXAFS results.
$D_{CO_{chemisorption}}$: fraction of atoms on the surface of Pd clusters calculated from CO chemisorption results.
[a] CO chemisorption measurements were carried out in ASAP 2010 micromeritics.

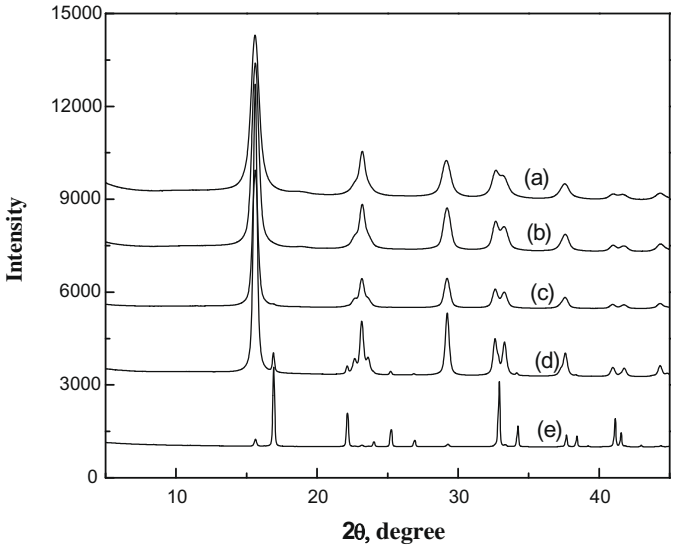

Fig. 4a. Powder X-ray diffraction patterns of TiO_2 nanoparticles prepared by hydrolysis of titanium butoxides followed by calcination at various temperatures: (a) 300, (b) 350, (c) 450, (d) 550, and (e) 650 °C.

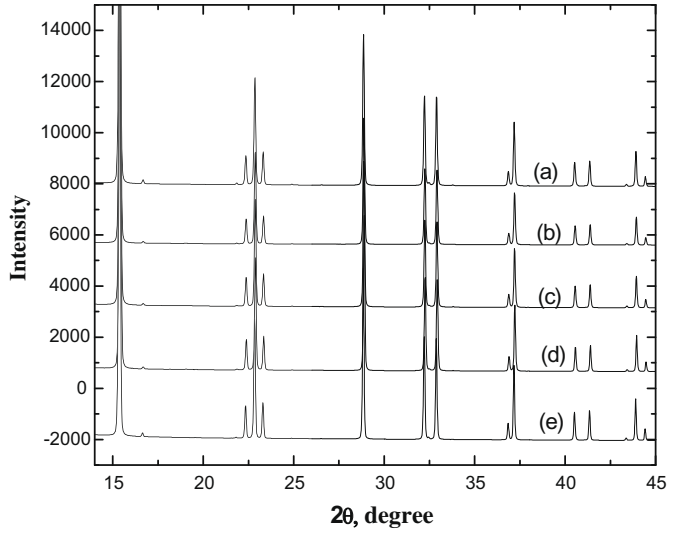

Fig. 4b. Powder X-ray diffraction patterns of commercial anatase nanoparticle B heated at various temperatures: (a) room temperature, (b) 350, (c) 450, (d) 550, and (e) 650 °C.

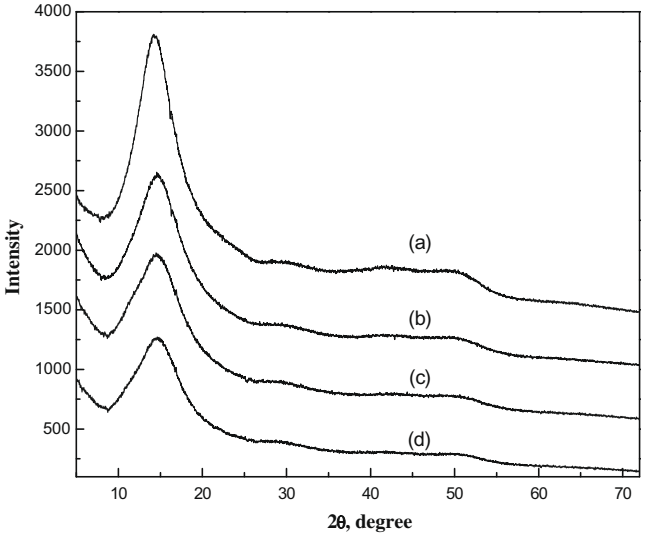

Fig. 5a. Powder X-ray diffraction patterns of SiO_2 heated at various temperatures: (a) room temperature, (b) 450, (c) 600, and (d) 900 °C.

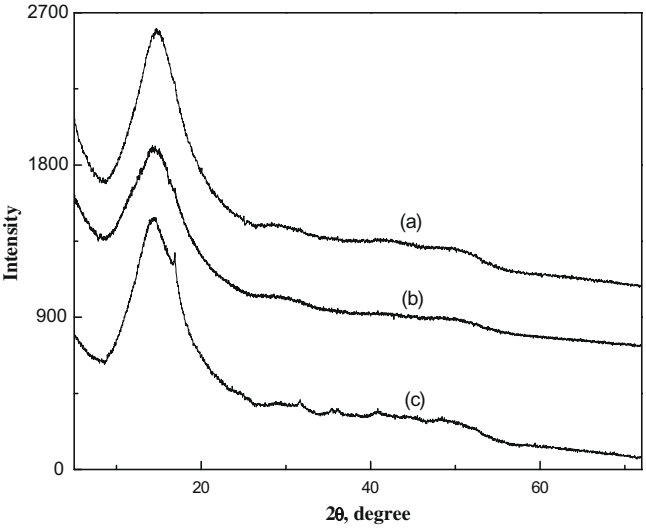

Fig. 5b. Powder X-ray diffraction patterns of anatase TiO_2 in TiO_2–SiO_2 heated at various temperatures: (a) 450, (b) 600, and (c) 900 °C.

mated from Nyquist theorem [7]: $n = (2\Delta k \Delta r/\pi) + 1$, where Δk and Δr, respectively, are the *k range* and *r* range used in the forward and inverse Fourier transforms ($\Delta k = 9$ Å^{-1} and $\Delta r = 2.5$ Å). The coordination number characterizing the TiO_2–SiO_2 interface (Ti–Si), namely 2.4, suggests that at least 60% of TiO_2 existed at the interface between TiO_2 clusters and SiO_2. The Ti–Ti coordination number of 3.0 further suggests that layer-like clusters of average diameter less than 25 Å were formed on SiO_2 support. The proposed structure model is consistent with PXRD characterizing the morphology of species with crystal grain sizes less than 40 Å; no characteristic peaks were observed in PXRD (Fig. 5b).

3.5. Role of grafted TiO_2 in improving Pd dispersion

EXAFS data of PdO_x/TiO_2–SiO_2, PdO_x/TiO_2, and PdO_x/SiO_2 samples before reduction are shown in Fig. 8. After Pd–Pd phase-corrected Fourier transformation was performed on the spectra, a peak at about 3.2 Å was observed for the PdO_x/SiO_2 and PdO_x/TiO_2 samples. In contrast, two small peaks appeared at about 3.0 and

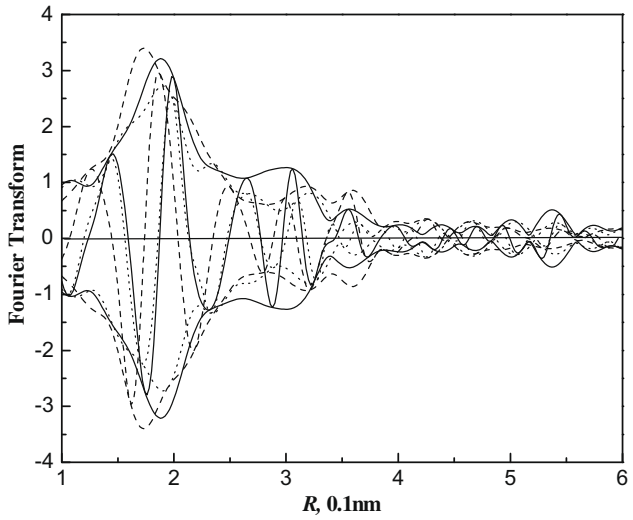

Fig. 6. Magnitude and imaginary part of the EXAFS Fourier transform ($3.5 < k^3 < 14.0$, Ti–O phase corrected) for $Ti(OCH(CH_3)_2)_4$ (dashed line), $Ti(OCH(CH_3)_2)_4$ adsorbed on SiO_2 (dotted line), and TiO_2–SiO_2 (solid line).

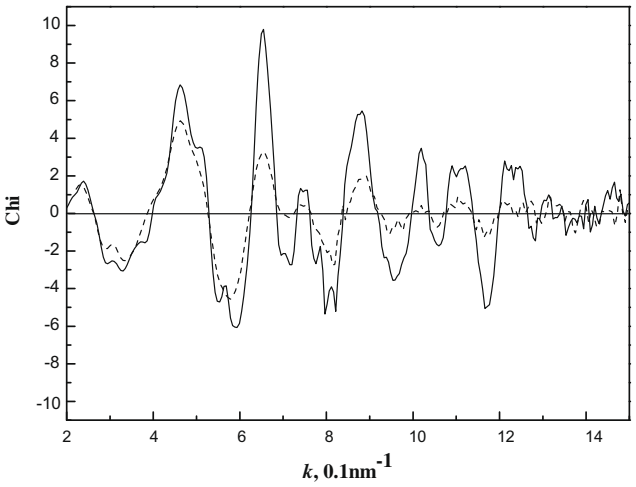

Fig. 7a. Raw EXAFS data (k^3 weighting) for commercial anatase with crystal grain size less than 100 nm (solid line) and TiO_2–SiO_2 (dashed line).

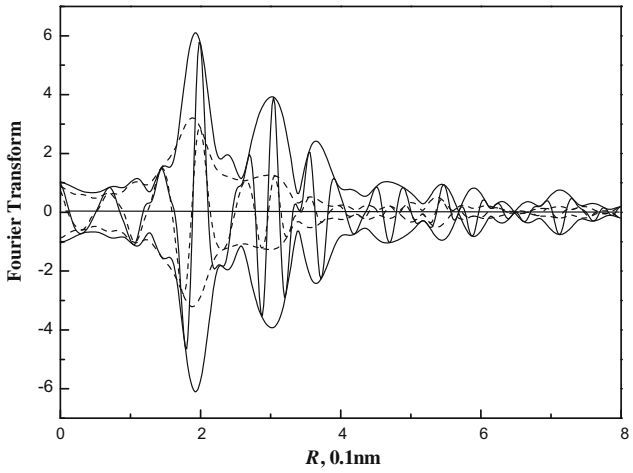

Fig. 7b. Comparison of the imaginary and magnitude of Fourier transform ($3.5 < k^3 < 14.0$, Ti–O phase corrected) of EXAFS data between commercial anatase with crystal grain size less than 100 nm (solid line) and TiO_2–SiO_2 (dashed line).

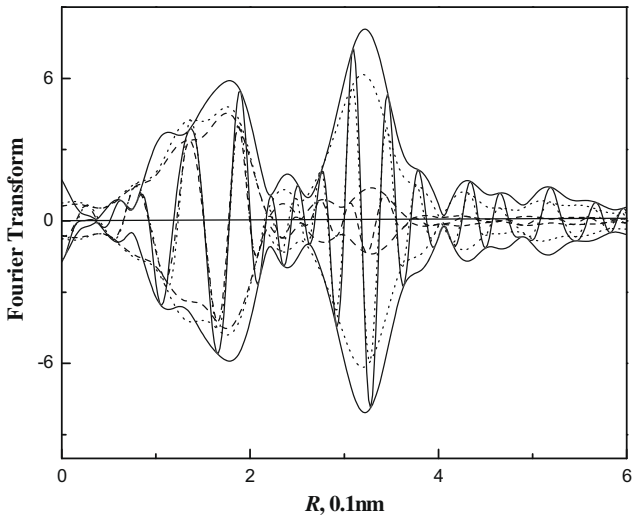

Fig. 8. Magnitude and imaginary part of the EXAFS Fourier transform ($3.2 < k^2 < 12.0$, Pd–Pd phase and amplitude corrected) for PdO_x/TiO_2–SiO_2 (dashed line), PdO_x/SiO_2 (dotted line), and PdO_x/TiO_2 (solid line).

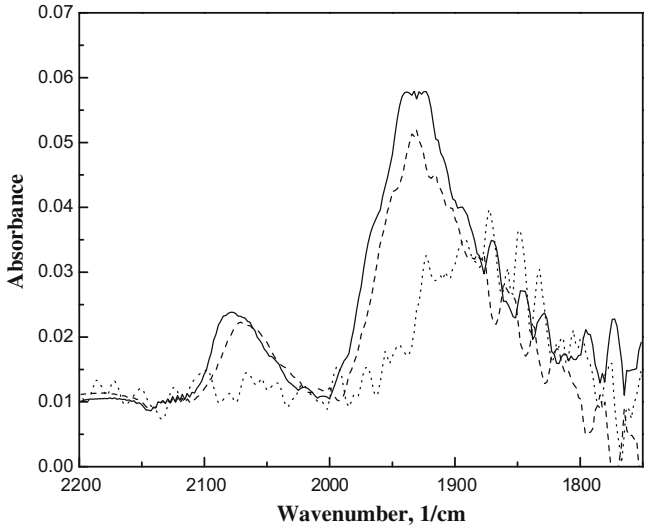

Fig. 9. Infrared spectra in the CO-stretching region characterizing CO adsorbed on Pd/TiO_2–SiO_2 (solid line), Pd/SiO_2, (dashed line), and Pd/TiO_2 (dotted line).

3.3 Å for PdO_x/TiO_2–SiO_2 (Fig. 8). Detailed EXAFS analysis showed that the PdO_x/SiO_2, PdO_x/TiO_2, and PdO_x/TiO_2–SiO_2 samples all have average Pd–O and Pd–Pd bond distances of about 2.0 Å and 3.1 Å, respectively, which are consistent with the first and second shells of PdO (within 0.1 Å deviations) [29]. The result indicates that the formation of PdO phase concomitantly with the aggregation during air calcination. Moreover, Pd–Pd coordination numbers estimated from EXAFS data were 5.4, 3.9, and 1.8 for PdO_x/TiO_2, PdO_x/SiO_2, and PdO_x/TiO_2–SiO_2, respectively, indicating that PdO on TiO_2–SiO_2 had the lowest aggregation rate among the three supports.

Because the peaks characterizing Pd–Ti and Pd–Si for PdO_x/TiO_2–SiO_2 are rather small, identifying the nature of backscattering of Si and Ti is difficult. Hence, model discrimination technique was used to fit the EXAFS data, and the results indicated that both Pd–Ti and Pd–Si contributions should be included in the model in order to give the best statistical fit. Based on the structure model, the rather high dispersion of PdO on TiO_2–SiO_2 support could be explained by the facts that (1) layer-like TiO_2 clusters anchor PdO and maintains it in a high dispersion during calcination and (2) the increase of SiO_2 surface roughness due to the presence of TiO_2 aggregates retards the aggregation of PdO.

Compared to TiO_2–SiO_2, the surface area of TiO_2 nanoparticles is much smaller; hence, it is easier for PdO to aggregate on the surface of TiO_2 nanoparticles and form much bigger clusters.

3.6. FT-IR characterizing the CO adsorbed on the Pd catalysts

IR spectra of Pd/TiO_2–SiO_2, Pd/SiO_2, and Pd/TiO_2 indicate that the former two catalysts have two CO absorption sites at about 2070 and 1930 cm^{-1}, while Pd/TiO_2 has only one absorption site at a low frequency of 1900 cm^{-1} (Fig. 9). The IR spectra are consistent with the spectra reported in the literature [31–33]. The band at about 2060–2080 cm^{-1} was assigned as the terminal CO adsorbed on Pd particles, and the absorption peak located at about 1880–1930 cm^{-1} was assigned to the bridged CO.

When CO is adsorbed on Pd clusters, electron transfer occurs from the d-orbital of the Pd to π^*(anti-bonding) orbital of CO. Less electronic density on Pd sites causes less back donating from Pd to the CO π^* orbital. This back donating strengthens the Pd–C bond and weakens the C–O bonding [12,31]. Hence, the difference of υ_{CO} absorption band may relate to the electronic properties of the Pd active sites available on the surface [31–33].

Pd active sites of high coordination are expected to have more electronic density than those of low coordination. As the back-donation character of the Pd–C bond increases, the C–O bond becomes weaker, together with a lower υ_{CO} absorption frequency. Hence, the adsorption of CO onto sites of high coordination would result in a bridged υ_{CO} absorption peak, while that onto low coordination sites would result in a terminal υ_{CO} absorption peak [31]. In addition, as shown in Fig. 9, the bridged υ_{CO} absorption bands are broad and present more diverse frequencies than terminal υ_{CO} absorption bands. This result may suggest that Pd atoms in high coordination sites are more variable in bonding character than those in low coordination sites.

CO adsorbed on single crystals of various orientations [34,35] and those obtained on supported Pd [33,36] were studied extensively using IR reflection spectroscopes. These studies showed that at a high coverage of CO, the bands of bridged-bonded CO are located at higher frequencies on Pd(100) planes when compared with Pd(111) planes. The difference of metallic coordination between Pd(100) and Pd(111) planes accounts for this behavior. Both terminal and bridged υ_{CO} absorption peaks of Pd/TiO_2–SiO_2 are approximately 10 cm^{-1} higher than those of Pd/SiO_2 sample, and the bridging υCO absorption peak of Pd/SiO_2 is approximately 30 cm^{-1} higher than that of Pd/TiO_2 (Fig. 9). The results may suggest that the densities of Pd(100) orientation on the Pd clusters for the three samples are in the order: Pd–TiO_2–SiO_2 > Pd–SiO_2 > Pd–TiO_2.

A strong correlation that existed between the electronic density and the metal cluster size of a nanometer-scale has been reported by Bazin et al. through ab initio calculation [37] and evidenced by the correlation between Pd cluster size and the binding energy of the Pd $3d_{5/2}$ [38]. It was found that the electronic density of metal clusters is proportional to the cluster size. Combination of our FT-IR, TEM, and EXAFS results showed that the frequency of υ_{CO} absorption peaks increases with the decrease of Pd cluster size (Figs. 3 and 9 and Tables 1 and 2). The shift of υ_{CO} absorption peaks to higher frequency and the increase of terminal-to-bridged CO intensity characterized by FT-IR with decreasing Pd cluster size can thus be explained by the correlation reported by Bazin et al. [37].

The effects of metal–support interactions may not be ruled out because the interaction between support and metal clusters is also related to the electronic density [39,40]. The Pd clusters may be viewed as a source of electron density, while support may be

viewed as an electron acceptor. The increase of metal–support interaction may deplete the electronic density of Pd clusters resulting in a decrease of bridged υ_{CO} absorption peak intensity; as shown in Fig. 9, terminal-to-bridged CO intensities for the three catalyst samples are in the order: Pd/TiO_2–SiO_2 > Pd/SiO_2 > Pd/TiO_2.

3.7. Effects of Pd morphology on sulfur poisoning and hydrogen reactivation

As shown in Figs. 1 and 9, two deactivation stages and two υ_{CO} absorption bands were observed for Pd/TiO_2–SiO_2 and Pd/SiO_2 samples, while only one was observed for Pd/TiO_2. Accordingly, we proposed that there are two different types of active sites on SiO_2 and TiO_2–SiO_2 supports, whereas there is only one type on TiO_2. These two active sites were denoted as Pd_l and Pd_h, where the subscripts l and h are represented as active sites with low coordination and high coordination, respectively.

Active sites of high coordination may present a higher basicity toward the acidic hydrogen of H_2S. Thus the affiliation of H_2S on Pd_h site is higher than that on Pd_l site due to the difference of electronic density. This may result in a higher poisoning effect on the Pd_h site.

Sulfur poisoning of these two active sites could thus be formulated as:

$$Pd_l + H_2S \leftrightarrow Pd_l - H_2S \leftrightarrow Pd_lS + H_2 \quad (1)$$

$$Pd_h + H_2S \leftrightarrow Pd_h - H_2S \leftrightarrow Pd_hS + H_2 \quad (2)$$

Since Pd/TiO_2 exhibits only bridged υ_{CO} absorption band and no activity was left after 5-h poisoning, irreversible reaction was suggested for the sulfur-poisoning reaction. Eq. (2) was simplified as

$$Pd_h + H_2S \rightarrow Pd_hS + H_2 \quad (3)$$

In the case of Pd/TiO_2–SiO_2 and Pd/SiO_2 samples, we expected that the first-stage deactivation resulted from the formation of Pd_hS and the second stage resulted from the adsorption of H_2S on Pd_l and the formation of Pd_lS. However, inferring from the findings of Kim et al. that the formation of Pt–S bond induces Pt migration leading to a sintering of Pt clusters [41], we might expect that affinity of these two Pd sites for H_2S and their respective poisoning rates might be varied with the sintering effects. Because of the complexity of the sulfur-poisoning mechanism, rather than attempting to develop a rigorous model, we proposed an empirical model based on the observation of test reactions. In the model, rate expression for the competition adsorption was formulated by assuming that the adsorption rate of H_2S on Pd_l sites is inversely proportional to the number of vacant Pd_h. For simplification, the model also lumps the effects of Pd migration into deactivation constants.

In order to examine external mass transfer limitation, Pd/SiO_2 catalyst was tested at a constant WHSV ($12\ h^{-1}$) with variable superficial mass flow velocities, u_s, ranging from 25 to 80 g/$cm^2\ h^{-1}$; where u_s = (mass flow rate, g/h)/(inside cross section of the reactor, cm^2) (porosity of catalyst bed). The experimental results indicated that tetralin conversion did not vary (within experimental error) with superficial velocities; the tetralin conversions were 0.91, 0.94, and 0.92 for superficial mass velocities of 28, 42, and 84 g/$cm^2\ h^{-1}$, respectively. The results suggested that the external mass transfer limitation is insignificant [42].

Since the particle sizes of Pd/TiO_2, Pd/SiO_2, and Pd/TiO_2–SiO_2 are rather small, examination of the diffusion resistance of these is rather difficult. Hence, a model Pd/SiO_2 catalyst having a 4 mm diameter was purposely prepared by the use of pellet SiO_2 support (CARiACT Q10, SA = 300 m^2). When the catalyst was crushed from 4 mm to about 1 mm tetralin conversion increased from 0.68 to 0.91 for the superficial mass velocity of 42 g/$cm^2\ h^{-1}$. When the catalyst was further pulverized to about 0.2 mm, the conversion increased to 0.93. Since the diameters of Pd/SiO_2 and Pd/TiO_2–SiO_2 catalysts are of 0.2–0.5 mm and the pore diameters of these catalysts are close to that of the model catalyst, the internal-mass-transfer testing results suggested that the tests for the comparison of the stability of Pd/SiO_2 and Pd/TiO_2–SiO_2 should be operated in the regimes of combination of chemical and diffusion control, whereas the effectiveness factor η was greater than 0.9; η was estimated by the use of the correlation between η and generalized Thiele modulus [42].

Combined with the definition of activity function [42], the decay rate law [43], and the rate expression for tetralin hydrogenation proposed by Boudalt [44], a model for the sulfur-poisoning catalyst deactivation was formulated as follows:

$$\frac{dC_T}{d\tau} = -\frac{k_h C_{H_2} C_T}{1 + K_T C_T}\eta a_{sum} \approx k'_h C_T a_{sum}, \quad \text{when } K_T \gg 1 \quad (4)$$

$$\frac{da_h}{dt} = -k_{1f} a_h \quad (5)$$

$$\frac{da_l}{dt} = -\frac{k_{2f} a_l}{1 + K_b a_h} + k_{2r} a_l \quad (6)$$

$$\frac{da_l}{dt} = \frac{k_{2f} a_l}{1 + K_b a_h} - k_{2r} a_l - (k_{3f} a_l - k_{3r} a_{ls}) \quad (7)$$

$$a_{sum} = a_h + a_l, \text{ at start of run, } a^0_{sum} = a^0_h + a^0_l = 1 \quad (8)$$

$$a^0_l = a_l + a_{ls} + a_l \quad (9)$$

In Eq. (4) (design equation), τ (1/WHSV) is the space time; η is the overall effectiveness factor indicating the relative importance of mass transfer and reaction limitation; C_T and C_{H_2} are the concentrations of tetralin and hydrogen, respectively; K_T is the adsorption equilibrium constant of tetralin; k_h is the intrinsic hydrogenation reaction constant; and a_{sum} is the normalized total activity coefficient and is equal to the summation of activity coefficient of high coordination sites, a_h, and low coordination sites, a_l. Since hydrogen concentration in the liquid phase is dependent on the reaction pressure and temperature, which assure constants during the tests, k_h can thus be lumped with C_{H_2} and η, and it becomes $k_{h'}$. When K_T is much less than 1, the design equation can be simplified as a pseudo-first-order rate expression, which is consistent with the model reported by Castaño et al. [45].

Eq. (5) was derived based on Eq. (3), where a_h is the catalytic activity contributed from high coordination sites, and k_{1f} is a rate constant for describing the loss of catalyst activity due to the formation of Pd_hS.

Eqs. (6), (7) and (9) were derived based on Eq. (1), where a_l is the catalytic activity contributed from low coordination sites, a_l is the activity loss due to the adsorption of H_2S on low coordination sites, and a_{ls} is the activity loss caused by the formation of Pd_lS. The kinetic constants k_{2f} and k_{2r} are the forward and reverse rate constants of H_2S adsorbed on the low coordination sites, respectively, and k_{3f} and k_{3r} are the forward and reverse rate constants for the formation of Pd_lS, respectively; where K_b is a parameter for assessing the importance of Pd_h in retarding H_2S adsorbed on Pd_l. The accelerated deactivation data (Fig. 1) were fitted by the proposed model with the least-square criteria, and the results are summarized in Table 3.

It is worthy to note that the activity improvement contributed by the grafted TiO_2 as assessed by the ratio of observed rate constants, $k'_{h(Pd/TiO_2-SiO_2)}/k'_{h(Pd/SiO_2)}$, will be underestimated. In testing Pd/SiO_2 and Pd/TiO_2–SiO_2 catalysts, the geometry of the catalyst pellets and the operating conditions are the same for these two catalysts tested, while the pore radius of the Pd/TiO_2–SiO_2 catalyst is slightly smaller than that of Pd/SiO_2. Thus, the effective diffusivity and the corresponding overall effectiveness factor η for Pd/TiO_2–SiO_2 are slightly smaller than those for Pd/SiO_2. Based on

Table 3
Summary of fitting results.

Parameter	$Pd/TiO_2–SiO_2$	Pd/SiO_2	Pd/TiO_2
k'_h (g of feed/h * g_s of catalyst)	55	32	16
TOF (molecules/s * surface atom)	0.93	0.70	0.78
a_b^0	0.49	0.56	1.0
k_{1f}	0.015	0.017	0.017
k_{2f}	1.4	1.6	–
k_{2r}	2.4	2.3	–
k_{3f}	0.61	0.83	–
k_{3r}	0.050	0.003	–
K_b	3600	3500	–

TOF is calculated based on k'_h; the value will be a little bit higher (about 10%) if diffusion resistance is considered.

Eq. (4), ratio of intrinsic rate for $Pd/TiO_2–SiO_2$ to that for Pd/SiO_2, $k_{h(Pd/TiO_2-SiO_2)}/k_{h(Pd/SiO_2)}$, will be slight higher than the ratio of the observed rate constant, $k'_{h(Pd/TiO_2-SiO_2)}/k'_{h(Pd/SiO_2)}$.

Turn over frequency (*TOF*) is the number of molecules reacting per active site per second under the conditions of the experiment [43]. In this study, atoms on the surface of Pd clusters were considered as active sites. Based on the rate constant k'_h and D_{EXAFS}, the *TOFs* were calculated, and the results indicated that *TOF* for $Pd/TiO_2–SiO_2$ is higher than those of the other two catalysts (Table 3). Inferring from the report by Williams et al. [40], we suggest that the higher catalyst activity for $Pd/TiO_2–SiO_2$ may be attributed to the more depletion in electron density of Pd clusters caused by the higher metal–support interactions and/or smaller Pd clusters. However, the detailed chemistry needs to be studied further.

According to the correlation between Pd cluster size and the affinity of Pd for H_2S discussed above, we first expected that the exhibition of better catalytic performance by $Pd/TiO_2–SiO_2$ was mainly because of the less H_2S being adsorbed. The fitting results were not completely consistent with our first expectation. As shown in Table 3, k_{2f}/k_{2r} for Pd/SiO_2 is only slightly higher than that for $Pd/TiO_2–SiO_2$, while k_{3f}/k_{3r} for Pd/SiO_2 is more than 20 times that for $Pd/TiO_2–SiO_2$. Moreover, fitting results showed that k_{3r} for $Pd/TiO_2–SiO_2$ is about 17 times that for Pd/SiO_2. Based on the results, we suggest that PdS species on $TiO_2–SiO_2$ present much higher hydrogen reducibility than those on SiO_2. However, the suggestion is not conclusive because the deactivation model is simplified as there may be a variety of models rather than just one model which can fit the experimental data.

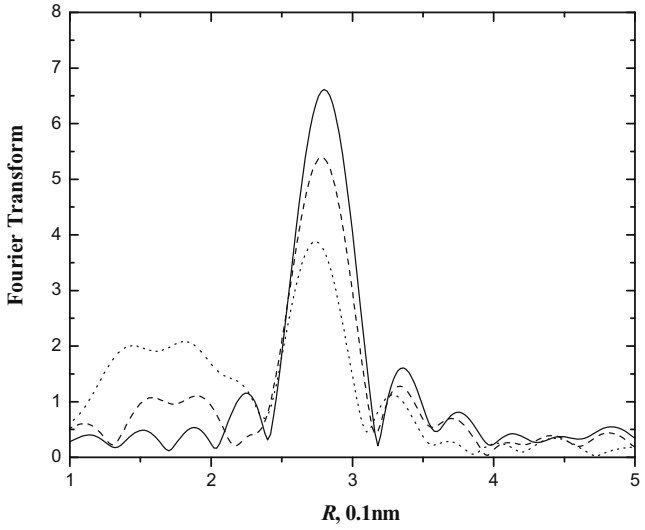

Fig. 10a. Magnitude of the EXAFS Fourier transform ($3.0 < k^2 < 12.0$, Pd–Pd phase and amplitude corrected) for $Pd/TiO_2–SiO_2$ (solid line), $PdO_x/TiO_2–SiO_2$ after H_2S treatment (dotted line), and $PdO_x/TiO_2–SiO_2$ after H_2S treatment followed by hydrogen reactivation (dashed line).

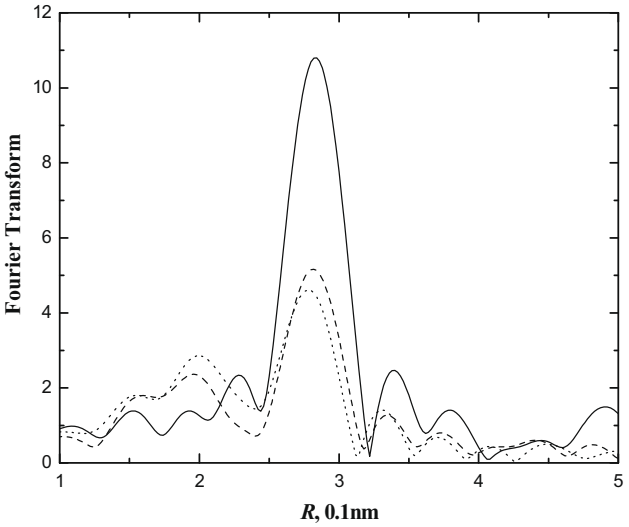

Fig. 10b. Magnitude of the EXAFS Fourier transform ($3.0 < k^2 < 12.0$, Pd–Pd phase and amplitude corrected) for Pd/SiO_2 (solid line), PdO_x/SiO_2 after H_2S treatment (dotted line), and PdO_x/SiO_2 after H_2S treatment followed by hydrogen reactivation (dashed line).

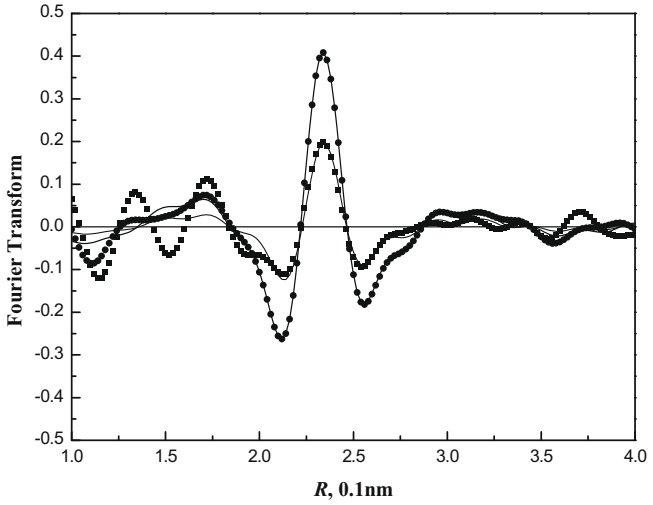

Fig. 10c. Comparison of the imaginary Fourier transform ($3.0 < k^2 < 12.0$, Pd–S phase corrected) of Pd–S EXAFS contribution between $Pd/TiO_2–SiO_2$ (■) and Pd/SiO_2.

To further confirm the conclusions derived from the kinetic study, sulfur tolerance and hydrogen reducibility of $Pd/TiO_2–SiO_2$ and Pd/SiO_2 were examined by EXAFS. Since the catalyst samples are air sensitive, in-situ EXAFS experiments were performed with exclusion of air and moisture.

As shown in the Figs. 10a and 10b, after sulfur poisoning, the peak intensities characterizing Pd–Pd contribution decrease with an appearance of a new peak at about 1.9 Å. The peak can be identified by subtracting the estimated Pd–Pd and $Pd–O_{support}$ contributions from the experimental EXAFS function. The Pd–S phase-corrected Fourier transforms of the difference file were calculated, resulting in a symmetric peak in the imaginary part. The observation is consistent with the identification of the backscattering atom as S (Fig. 10c). The detailed EXAFS analysis shows that the new peak reveals a bond distance of 2.30 ± 0.04 Å, which is consistent

with the crystallographic data of PdS_2 [29]. Based on Eqs. (1) and (2), the higher Pd–S contribution for Pd/SiO_2 (Fig. 10c, Table 1) indicates that the catalysts exhibit relatively higher H_2S adsorption and/or surface reaction rate than $Pd/TiO_2–SiO_2$. These results suggest that H_2S has a higher affinity for Pd/SiO_2. In addition, it might be caused by the roughness of $TiO_2–SiO_2$ surface; no evidence indicates sulfur-poisoning-induced Pd aggregation.

Sulfur-poisoned $Pd/TiO_2–SiO_2$ and Pd/SiO_2 catalysts were reactivated with hydrogen at 200 °C to examine the difference of hydrogen reducibility; the temperature was chosen because the test reactions were run at 200 °C. After the treatments, about 80% of the peak intensity characterizing the Pd–Pd contribution of $Pd/TiO_2–SiO_2$ was recovered concomitantly with a decrease of 70% Pd–S contribution. In contrast, only a small fraction of PdS_2 on SiO_2 was converted to Pd after the treatments.

Detailed EXAFS analysis results confirm the conclusion derived from kinetic study that the superior activity maintenance for $Pd/TiO_2–SiO_2$ is not only due to the less H_2S adsorption rate but also due to the higher PdS_2 reducibility. After sulfur poisoning, Pd–Pd coordination numbers decrease from 5.7 to 3.2 for $Pd/TiO_2–SiO_2$, and from 7.8 to 3.2 for Pd/SiO_2. After hydrogen reactivation, the coordination numbers increase from 3.2 to 5.1 for $Pd/TiO_2–SiO_2$, and from 3.2 to 4.6 for Pd/SiO_2 (Table 1). Analysis results of Pd–S shell are consistent with those of Pd–Pd shell. Pd–S coordination number decreases from 0.7 to 0.2 for $Pd/TiO_2–SiO_2$, while it decreases from 1.5 to 1.4 for Pd/SiO_2 (Table 1).

The detailed chemistry whereby grafted-TiO_2 enhances sulfur resistance remains to be elucidated. Our observation and the published results of Guenin et al. [46] suggest a role of Pd cluster size. The layer-like TiO_2 clusters help anchoring the Pd and/or increase the roughness of SiO_2 surface, thereby maintaining Pd in high dispersion. The decrease of Pd clusters decreases the affinity of H_2S for Pd clusters while increasing the hydrogen reducibility of PdS_2, resulting in an increase of stability maintenance. However, we cannot rule out other factors such as Ti atoms inserting in the network of Pd, synergy effects [19,47], partial reduction of TiO_2 [48], and the interaction between Pd and Ti^{4+} [49].

4. Conclusions

The merits of the grafted TiO_2 in improving sulfur resistance were demonstrated by the comparison of the stability maintenance of Pd/TiO_2, $Pd/TiO_2–SiO_2$, and Pd/SiO_2 catalyst samples during sulfur-poisoning catalyst deactivation. With the combination of the complementary characterization techniques, namely XRD, EXAFS, TEM, and FT-IR, as well as catalytic performance tests, we suggest that the superior activity maintenance for the $Pd/TiO_2–SiO_2$ catalyst is not only due to less H_2S being adsorbed, but also due to the higher hydrogen reactivation rate. Based on kinetic study and EXAFS results, we suggest that PdS_2 contained in the smaller Pd clusters presents a higher reduction rate, which is consistent with the non-catalytic gas–solid reduction reaction kinetics. The lower H_2S affinity for Pd clusters on $TiO_2–SiO_2$ could also be explained by the relatively small Pd clusters, and the role of the grafted TiO_2 in maintaining the small Pd clusters was investigated by exploring the genesis of Pd clusters. The results indicated that the high thermal stability, high surface area of $TiO_2–SiO_2$ support, and anchoring Pd species on the support play the roles.

Acknowledgments

The EXAFS data were analyzed using the FEFF and XDAP Data Analysis Program. XDAP program was developed by M. Vaarkam, J.C. Linders, and D.C. Koningsberger. The support of the National Science Council of the Republic of China (Contract No. NSC-95-2221-E-194-079), National Synchrotron Radiation Research Center (NSRRC), Academia Sinica, and the Refining and Manufacturing Research Center of the Chinese Petroleum Corp. is acknowledged.

References

[1] B.C. Gates, Catalytic Chemistry, John Wiley & Sons, Inc., 1992. p. 378.
[2] B.C. Gates, J. Mol. Catal. A Chem. 163 (2000) 55.
[3] D.C. Koningsberger, B.C. Gates, Catal. Lett. 14 (1992) 271–277.
[4] V. Idakiev, L. Ilieva, D. Andreeva, J.L. Blin, L. Gigot, B.L. Su, Appl. Catal. A: Gen. 243 (2003) 25.
[5] N.S. de Resende, J.-G. Eon, M. Schmal, J. Catal. 183 (1999) 6.
[6] D. Bazin, J.J. Rehr, J. Phys. Chem. B 107 (2003) 12398.
[7] D.C. Koningsberger, R. Prins, X-ray Absorption: Principles, Applications, Techniques of EXAFS, SEXAFS, and XANES, Wiley, New York, 1988, p. 221, 395.
[8] Zbigniew Karpiński, Catalysis by supported, unsupported, and electron-deficient palladium, Adv. Catal. 37 (1990) 45–100.
[9] T.-B. Lin, T.C. Chou, Appl. Catal. A 108 (1994) 7.
[10] E.K. Novakova, L. McLaughlin, R. Burch, P. Crawford, K. Griffin, C. Hardacre, P. Hu, D.W. Rooney, J. Catal. 249 (2007) 93.
[11] S.H. Choi, J.S. Lee, J. Catal. 193 (2000) 176.
[12] F.A. Cotton, G. Wilkinson, Advance Inorganic Chemistry, John Wiley & Son, Inc., 1988, p. 924.
[13] C. Song, X. Ma, Appl. Catal. B 41 (2003) 207.
[14] J.A. Rodriguez, A.J. Hrbek, Acc. Chem. Res. 32 (1999) 719.
[15] J.K. Lee, H.K. Rhee, J. Catal. 177 (1998) 208.
[16] D. Hamilton, US Patent 4,640,764, 1987.
[17] K. Thomas, C. Binet, T. Chevreau, D. Cornet, J.-P. Gilson, J. Catal. 212 (2002) 63.
[18] W.M.H. Schatler, A. Yu Stakheev, Catal. Today 12 (1992) 283.
[19] B. Pawelec, R. Mariscal, R.M. Navarro, S. van Bokhorst, S. Rojas, J.L.G. Fierro, Appl. Catal. A: Gen. 225 (2002) 223.
[20] A.N.-R. öthlisberger, R. Prins, J. Catal. 242 (2006) 207.
[21] J.T. Miller, B.L. Mojet, D.E. Ramaker, D.C. Koningsberger, Catal. Today 62 (2000) 101.
[22] D.C. Koningsberger, J. de Graaf, B.L. Mojet, D.E. Ramaker, J.T. Miller, Appl. Catal. A: Gen. 191 (2000) 205.
[23] W.-B. Su, M.-T. Tang, J.-R. Chang, Ind. Eng. Chem. Res. 44 (2005) 1677.
[24] A.P Hammersley, ESRF Internal Report, FIT2D V12.012 Reference Manual V6.0 ESRF98HA01T, 2004.
[25] B.D. Cullity, Elements of X-ray Diffraction, second ed., Addison Wesley Publishing Company, Massachusetts, 1978, p. 99.
[26] M. Vaarkamp, J.C. Linders, D.C. Koningsberger, Physica B 208–209 (1995) 159.
[27] A.L. Ankudinov, B. Ravel, J.J. Rehr, S.D. Conradson, Phys. Rev. B58 (1998) 7565.
[28] J.-F. Chiou, Y.-L. Huang, T.-B. Lin, J.-R. Chang, Ind. Eng. Chem. Res. 34 (1995) 4279.
[29] P. Villars, Basic Database for Crystal Structures Pauling File, National Institute for Materials Science (NIMS).
[30] R. Koziowski, R.F. Pettlfer, J.M. Thomas, J. Phys. Chem. 87 (1983) 5172.
[31] L.H. Little, Infrared Spectra of Adsorbed Species, Academic Press, 1996, p. 51.
[32] L.F. Liotta, G.A. Martin, G. Deganello, J. Catal. 164 (1996) 322.
[33] R.S. Monteiro1, Lıdia C. Dieguez, Martin Schmal, Catal. Today 65 (2001) 77.
[34] A.M. Bradshaw, F.M. Hoffmann, Surf. Sci. 72 (1978) 513.
[35] A. Ortega, F.M. Hoffman, A.M. Bradshaw, Surf. Sci. 119 (1982) 79.
[36] A. Palazov, G. Kadinov, C. Bonev, D. Shopov, J. Catal. 74 (1982) 44.
[37] D. Bazin, D. Sayers, J. Rher, J. Phys. Chem. B 101 (1997) 11040.
[38] Yu. A. Ryndin, M.V. Stenin, A.I. Boronin, V.I. Bukhtiyarov, V.I. Zaikovskii, Appl. Catal. 54 (1989) 277.
[39] C. Woltz, A. Jentys, J.A. Lercher, J. Catal. 237 (2006) 337.
[40] M.F. Williams, B. Fonfé, C. Woltz, A. Jentys, J.A.R. van Veen, J.A. Lercher, J. Catal. 237 (2006) 337.
[41] D.H. Kim, J.H. Kwak, J. Szanyi, S.J. Cho, C.H. Peden, J. Phys. Chem. C 112 (2008) 2981.
[42] G.F. Froment, K.B. Bischoff, Chemical Reactor Analysis and Design, John Wiley & Sons, Inc., 1990. p. 173, 163, 221.
[43] H.S. Fogler, Elements of Chemical Reaction Engineering, Prentice-Hall International, Inc., 1999, p. 634.
[44] M. Boudart, Chem. Eng. Prog. 58 (1962) 73.
[45] P. Castaño, D.V. Herk, M.T. Kreutzer, J.A. Moulijn, M. Makkee, Appl. Catal. B: Environ. (2008).
[46] M. Guenin, M. Breysse, R. Fret, K. Tifouti, P. Marecot, J. Barbier, J. Catal. 105 (1987) 144.
[47] J.-Y. Luo, M. Meng, X. Li, X.-G. Li, Y.-Q. Zha, T.-D. Hu, Y.-N. Xie, J. Zhang, J. Catal. 254 (2008) 310.
[48] S.D. Lin, C. Song, Catal. Today 31 (1996) 93.
[49] K. Ito, T. Tomino, M. Ohshima, H. Kurokawa, K. Sugiyama, H. Miura, Appl. Catal. A 249 (2003) 19.